

## Nanobubbles as corrosion inhibitor in acidic geothermal fluid

Aikawa, Asuki

Department of Earth Resources Engineering, Kyushu University

Kioka, Arata

Department of Earth Resources Engineering, Kyushu University

Nakagawa, Masami

Department of Earth Resources Engineering, Kyushu University

Anzai, Satoshi

MCS Division, Anzaikantetsu Co. Ltd.

<https://hdl.handle.net/2324/4481575>

---

出版情報 : Geothermics. 89 (101962), 2021-01. Elsevier

バージョン :

権利関係 :



1 **Nanobubbles as corrosion inhibitor in acidic geothermal fluid**

2  
3 **Asuki Aikawa (1,5), Arata Kioka (1,4\*), Masami Nakagawa (1,2), Satoshi Anzai (3)**

- 4 1. Department of Earth Resources Engineering, Kyushu University, Fukuoka, Japan.  
5 2. Department of Mining Engineering, Colorado School of Mines, Golden, CO, USA.  
6 3. MCS Division, Anzaikantetsu Co. Ltd., Yokohama, Japan.  
7 4. Institut für Geologie, Leopold-Franzens-Universität Innsbruck, Innsbruck, Austria.  
8 5. Now at Gas Resources Department, Saibu Gas Co., Ltd., Fukuoka, Japan.

9 \*Correspondence: A. Kioka (kioka@mine.kyushu-u.ac.jp; +81.92.802.3343). Department of Earth  
10 Resources Engineering, Kyushu University, Fukuoka 819-0395, Japan.

11  
12  
13 **ABSTRACT (195/200 words)**

14 Metallic corrosion is a major issue that leads to an efficiency loss and eventual failure of the  
15 system in geothermal power plants. Despite the growing understanding of mechanisms of corrosion,  
16 inhibiting steel corrosion in the acidic geothermal fluids remains to present formidable challenges  
17 due to its intrinsic physicochemical complexity. Here, we study the use of nanobubbles as a possible  
18 corrosion inhibitor by testing alteration of the low-carbon steel plates immersed in acidic geothermal  
19 water with continuously injected air-nanobubbles. Nanobubbles have been used in a broad range of  
20 areas as they are eco-friendly, low-cost, easy-to-use and high-functional materials. We, for the first  
21 time to our knowledge, found that air-nanobubbles could inhibit steel corrosion, with inhibition  
22 efficiency of up to 50% in the studied acidic geothermal fluid. Air-nanobubbles could act as a  
23 nanoscopic coating material in the acidic geothermal fluid, through generating a bubble mattress  
24 and/or promoting nucleation and aggregation of a very small quantity of silica precipitation on the  
25 surface of steel plates. Our finding suggests that nanobubbles can inhibit steel corrosion in various  
26 chemically different geothermal fluids, highlighting the physicochemical significance of nanobubbles  
27 as the coating material for inhibiting metal degradation in the geothermal infrastructures.

28  
29 **KEYWORDS:** Nanobubbles; Steel corrosion; Corrosion inhibitor; Acidic geothermal fluid; Bubble  
30 mattress; Silica nanoparticle

31  
32  
33  
34  
35  
36  
37 Received 23 April 2020, Revised 27 August 2020, Accepted 28 August 2020.

38 <https://doi.org/10.1016/j.geothermics.2020.101962>

39 **HIGHLIGHTS**

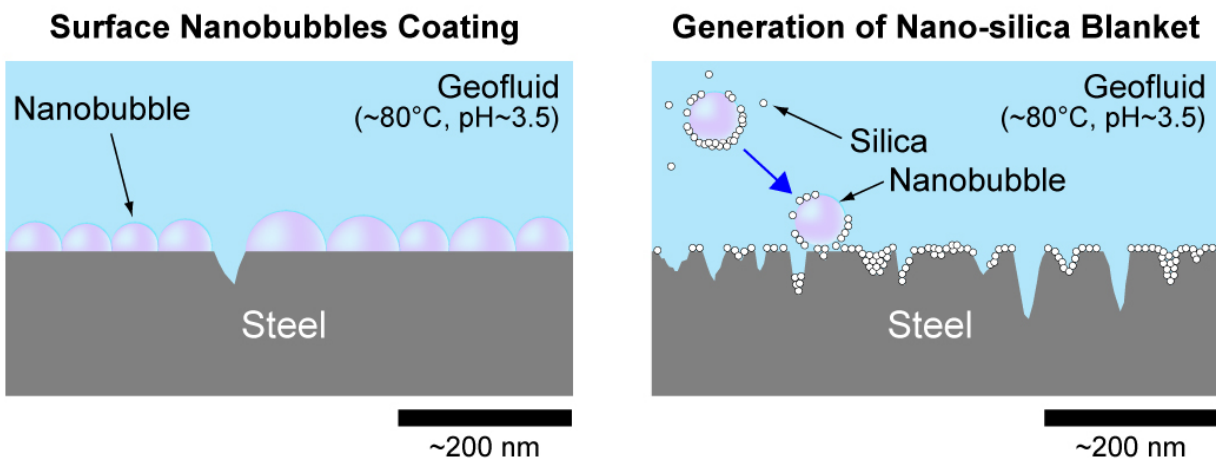
- 40 ✓ Corrosion testing of low-carbon steels immersed in an acidic geothermal fluid with injecting air-nanobubbles.
- 41
- 42 ✓ Air-nanobubbles facilitated the corrosion inhibition effectiveness of low-carbon steels of up to
- 43 50%.
- 44 ✓ Air-nanobubbles inhibited corrosion through bubble mattress and/or slight silica precipitation on
- 45 the steel surface.

46

47

48 **GRAPHICAL ABSTRACT**

49



50

51

52 **1. INTRODUCTION**

53 Nanobubbles with a typical diameter of 50–200 nm are currently a growing research area of  
54 broad disciplines, with a significant focus on understanding their nature in bulk aqueous solutions  
55 (Lohse and Zhang, 2015). Despite the growing understanding of the pivotal role of the nanobubbles,  
56 the comprehensive scientific understanding of the behavior of nanobubbles still remains poor and  
57 provides room for more investigation. In contrast to micrometer-sized bubbles, a noteworthy  
58 property of nanobubbles is their longevity in liquid solutions and stability at high temperatures.  
59 Nanobubbles can exist for many hours, several days, or even a couple of months (Michailidi et al.,  
60 2020) rather than milliseconds theoretically expected (Weijs and Lohse, 2013). Surface nanobubbles  
61 are stable with respect to a temperature increase up to the boiling point of bulk water (Zhang et al.,  
62 2014). Surface nanobubbles have also been recognized to make a strong impact on the solid-liquid  
63 interface as they change the two-phase contact to a three-phase contact. This includes the effect of  
64 surface nanobubbles that changes the wettability and slippage on the solid surface (Lauga and Stone,  
65 2003; Niavarani and Priezjev, 2010; Wang and Bhushan, 2010; Yen, 2015; Li et al., 2016). Thus, the  
66 use of nanobubbles holds promise in enabling to optimize the surface condition by controlling the  
67 interface hydrodynamically, allowing a broad range of engineering applications. Moreover, the use of  
68 nanobubbles will benefit from preventing chemical pollution and reducing cost for maintaining  
69 infrastructure in gas, oil, and geothermal industries, compared with the chemical products commonly  
70 used.

71 In geothermal infrastructures, material degradation due to corrosion is a major concern that  
72 leads to efficiency loss and eventual failure of the system. For example, steel instruments in the acidic  
73 geothermal fluid at moderate-to-high temperatures are subject to intensive corrosion (Nogara and  
74 Zarrouk, 2018a), increasing the operating costs of geothermal facilities. Well-planned material  
75 selection and corrosion engineering, taking into account environmental and economic considerations,  
76 are essential to reduce corrosion damage. It has been well documented that carbon steels, which are  
77 commonly used in a wide range of applications, are susceptible to intensive corrosion damages in  
78 highly corrosive geothermal fluids. In contrast, high-cost titanium, nickel and high nickel-based alloys,  
79 and (super-)ferritic and (super-)austenitic stainless steels have higher resistance levels to most  
80 geothermal fluid environments (Nogara and Zarrouk, 2018b). However, selecting the right materials  
81 presents a complex problem because the composition of geothermal fluids varies in a single operating  
82 day and from field to field. In addition to the costly corrosion-resistant material, numerous studies  
83 have alternatively sought to chemical solutions on the material surface for inhibiting corrosion. As  
84 the main corrosion process comprises anodic and cathodic reactions, corrosion inhibitors can  
85 generally be classified as anodic inhibitors, cathodic inhibitors, and mixed inhibitors (Tang, 2019). A  
86 protective coating of the material surface has also been found to be effective for inhibiting corrosion,  
87 by using microarc oxidation technologies (Sun et al., 2019) and organic compounds such as several  
88 Schiff base compounds (Shokry et al., 1998), acetylenic alcohols, propargyl alcohol and its derivatives  
89 (Finšgar and Jackson, 2014), Polyvinylamide derivatives (Tiu and Advincula, 2015), Pyridazinium

90 derivatives (El-Hajjaji et al., 2019), Imidazole and Imidazoline derivatives (Solomon et al., 2019; Sun  
91 et al., 2019). Despite such longstanding study efforts, steel corrosion remains to present daunting  
92 challenges due to its intrinsic complexity. As nanoscale corrosion pathways have been found to be a  
93 significant impact on the corrosion behavior of steel (Hayden et al., 2019), there is a growing demand  
94 for nanoscopic operations on effective mitigation of corrosion (Dwivedi et al. 2017). Therefore,  
95 nanobubbles are expected to be an effective additive that can inhibit steel corrosion nanoscopically  
96 in geothermal infrastructures.

97 Here, we investigate, for the first time to our knowledge, whether nanobubbles can inhibit  
98 steel corrosion in acidic geothermal fluids. We test corrosion of the mild-carbon steel specimens  
99 (coupons) immersed in acidic geothermal fluid on-site at a geothermal power plant, with injecting  
100 the nanobubbles continuously generated by air for 7 days. We examine the effectiveness of corrosion  
101 inhibition by air-nanobubbles, combined with weight loss measurements of the immersed coupons,  
102 and micro-morphological observations and chemical composition analyses on the surfaces of tested  
103 coupons. These data also allow to understanding mechanisms with respect to how nanobubbles  
104 inhibit nanoscopically the bulk steel corrosion in the acidic geothermal fluid. Nanobubbles hold the  
105 potential for being a novel, environment-friendly, inexpensive and easy-to-use approach for inhibiting  
106 steel corrosion in the intensively corrosive medium.

107

108

109

## 110 **2. METHODS AND MATERIALS**

111

### 112 **2.1. Experimental setup for on-site immersion corrosion tests**

113 The immersion corrosion testing was conducted on-site at the Hatchobaru Geothermal  
114 Power Plant (Kyushu Electric Power Co., Inc.) in Oita Prefecture, Japan. We used acidic geothermal  
115 fluid exiting the separator of the power plant (Figure 1), and its chemical composition and electrical  
116 conductivity are summarized in Table 1. The silica concentration was around 860 mg/L. The test  
117 coupons for corrosion experiments were immersed in the geothermal fluid overflowed continuously  
118 in two heat-resisting polypropylene containers (700 × 330 × 350 mm). The geothermal fluid in the  
119 containers was evenly stirred by small water pumps. The goal here is to investigate whether  
120 nanobubbles can mitigate corrosion of steel in the acidic geothermal fluid. Thus, two different fluid  
121 environments were created in the respective fluid-filled containers at atmospheric pressure:  
122 untreated geothermal fluid (reference fluid) and geothermal fluid mixed with air-nanobubbles (Figure  
123 1). In this study, we continuously generated air-nanobubbles and injected into the geothermal fluid  
124 for tested 7 days, using an ultrafine pore ceramic-nozzle type nanobubble generator (Anzaikantetsu  
125 Co., Ltd., Yokohama, Japan) at 0.2 MPa controlled by an air compressor. The nanobubble generator  
126 produces  $3 \times 10^9$  bubbles per milliliter with a mean diameter of 85 nm. The temperature and pH of the  
127 geothermal fluid in the containers were within 75–85°C and 3.4–3.6, respectively, during the test

128 period. The flow rate into and out of the containers varied between 0.5 and 2.0 L/min because we  
 129 could not control the flow rates of geothermal fluid leaving the separator.

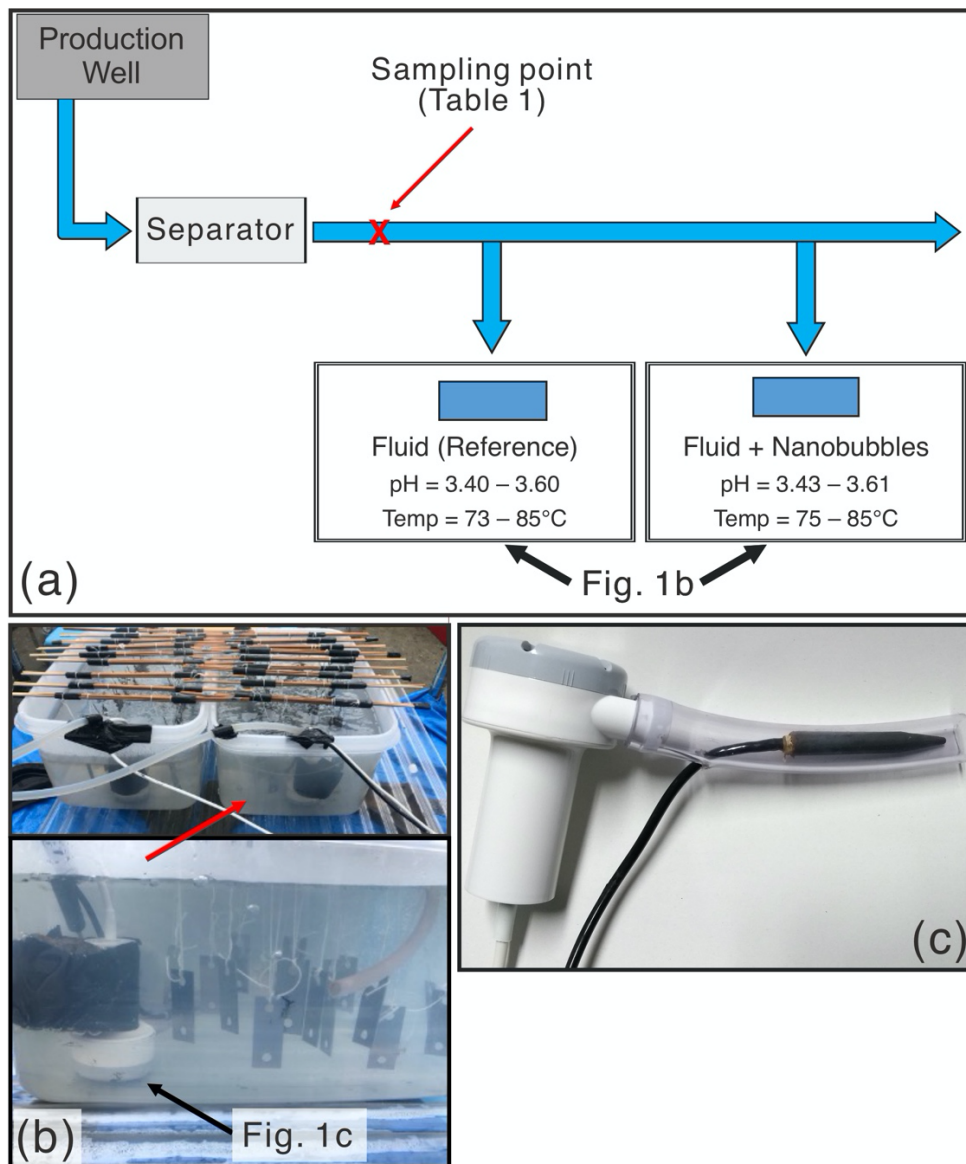
130

131

132 Table 1: Chemical composition (mg/L) and electrical conductivity (E.C.; mS/m) of studied geothermal  
 133 fluid (mg/L). The sampling point is shown in Figure 1a.

Na	K	Ca	Mg	Cl	SO <sub>4</sub>	HCO <sub>3</sub>	Fe	F	SiO <sub>2</sub>	E.C.
1090	198	8.0	360	1640	489	< 1	4027	4.3	855	617

134



135

136 Figure 1: (a) Schematic illustration of immersion corrosion experiments and sampling point of the  
 137 chemical properties of fluid listed in Table 1. (b) Photos of immersion corrosion experiments. (c)  
 138 Ceramic nozzle type nanobubble generator used in this study.

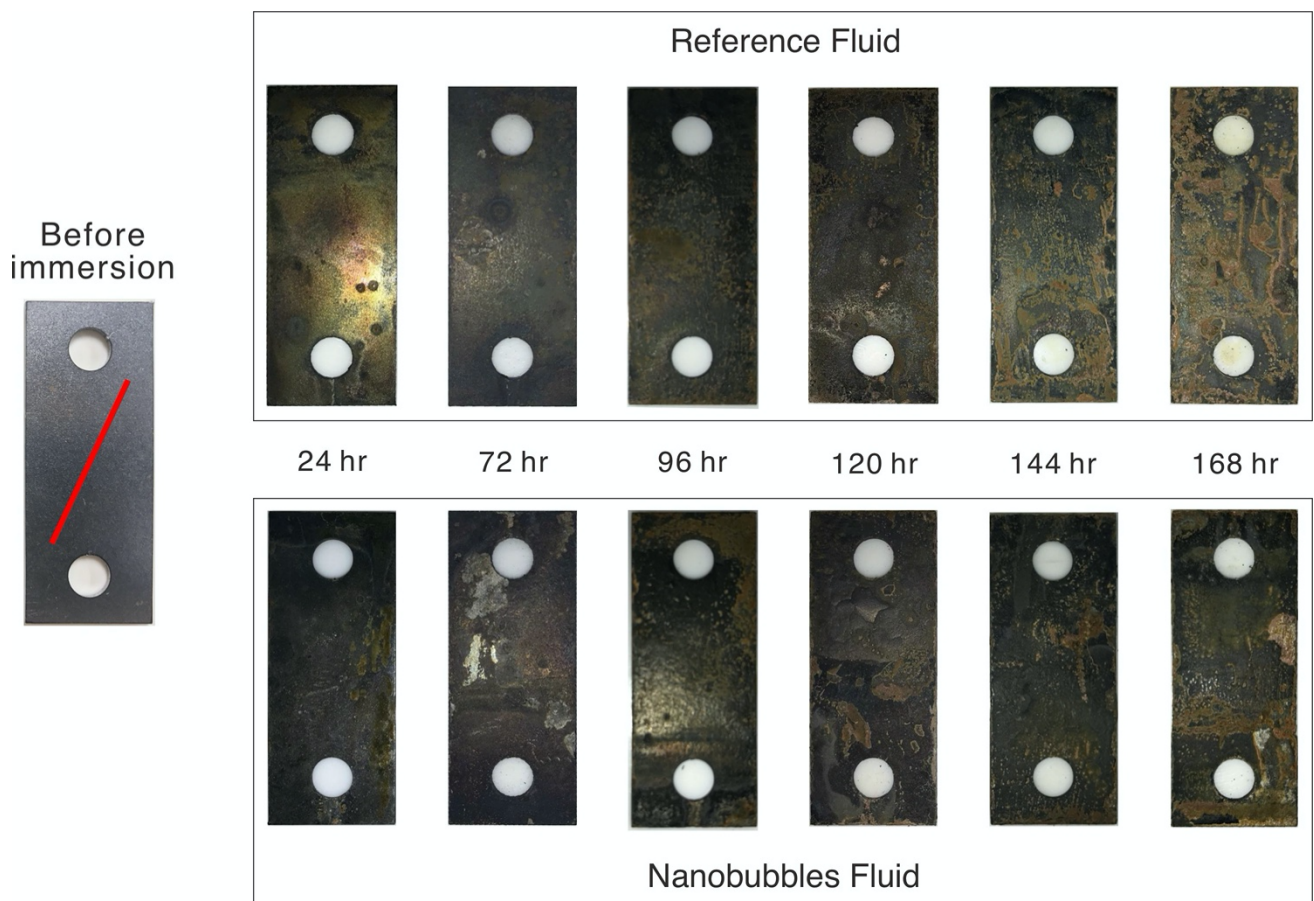
139

## 140 **2.2. Material, weight loss measurements, and surface analyses of immersed coupons**

141 The studied material for corrosion tests was low-carbon steel “Steel Plate Cold Commercial  
142 (SPCC)” (JIS G3141 Standards) with the following chemical composition (wt%): C ≤ 0.15, Mn ≤ 0.10, P  
143 ≤ 0.10, S ≤ 0.035, few negligible impurities and the rest is Fe. The coupon for corrosion tests was  
144 fabricated according to the American Society for Testing and Materials (ASTM) standard G4-01  
145 “Standard Guide for Conducting Corrosion Tests in Field Applications” (ASTM G4-01, 2008). The test  
146 coupon was made from an SPCC steel plate and had two 6.5-mm diameter holes (Figure 2), and its  
147 dimension was 50 × 20 × 1.1 mm (length × width × thickness). The rectangular coupon was fabricated  
148 by laser cutting. The 6.5 mm hole was used for dangling in the tested fluid using a PTFE-string  
149 connected to a hanging rod on the container (Figure 1b). All the coupons were weighed before  
150 immersion and ranged between 8654.8 and 8705.2 mg. We immersed all the coupons together either  
151 in the containers filled with reference fluid or nanobubbles fluid (Figure 1b) and identified the  
152 coupons by labeling on their hanging rod. Each immersed coupon was systematically taken out of the  
153 reference fluid and the fluid mixed with air-nanobubbles after 24, 48, 72, 96, 120, 144, and 168 hours.  
154 The coupon was cleaned immediately after removal from the fluid as advised by the ASTM standard  
155 G4-01 (ASTM G4-01, 2008). According to the ASTM standard G1-90 “Standard Practice for Preparing,  
156 Cleaning, and Evaluating Corrosion Test Specimens” (ASTM G1-90, 1999), the sampled coupon was  
157 rinsed carefully using distilled water to remove corrosion products, dried, and weighed to calculate  
158 the loss of its mass. To evaluate protection efficiency by mixing nanobubbles in the geothermal fluid,  
159 we calculated the corrosion inhibition effectiveness  $\eta(t)$  (%) of the coupons immersed in the air-  
160 nanobubbles fluid for  $t$  (hr):

$$161 \quad \eta(t) = \left( \Delta m_{ref}(t) - \Delta m_{nb}(t) \right) / \Delta m_{ref}(t) \times 100,$$

162 where  $\Delta m_{ref}(t)$  (g) and  $\Delta m_{nb}(t)$  (g) are the weight losses of the coupons immersed in the  
163 reference fluid and the air-nanobubbles fluid for  $t$  (hr), respectively. Here, a smaller weight loss of  
164 the coupon immersed in the air-nanobubbles fluid  $\Delta m_{nb}(t)$  indicates a better corrosion inhibition  
165 effectiveness by nanobubbles for a given time. In the laboratory, we analyzed surface microstructure  
166 of the weighed coupons by Scanning Electron Microscope (SEM) using a HITACHI SU3500 at Center of  
167 Advanced Instrumental Analysis, Kyushu University. We also determined the chemical composition of  
168 corrosion on the coupon surface by Energy-dispersive X-ray spectroscopy (EDX).  
169



170

171 Figure 2: Photos of the coupons from the reference fluid and air-nanobubble fluid after 24 hr, 72 hr,  
 172 96 hr, 120 hr, 144 hr, and 168 hr of immersion test. A red line in the photo of coupon before immersion  
 173 test (left) indicates the scanning position of EDX analyzes.

174

175

176

177 **3. RESULTS**

178

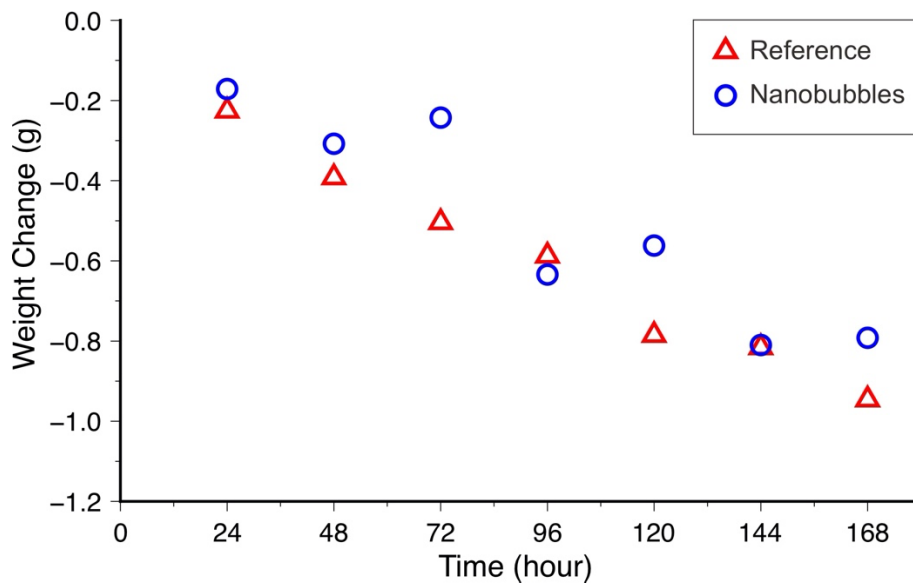
179 **3.1. Visual inspection and weight losses of immersed coupons**

180 Immersed coupons were sampled from the reference fluid and the fluid mixed with air-  
 181 nanobubbles after 24, 48, 72, 96, 120, 144, and 168 hours of immersion testing. Even after 24 hours  
 182 of immersion testing, both the coupons from the reference fluid and air-nanobubble fluid already lost  
 183 much of their metallic luster (Figure 2). Corrosion damages were then more significant in the coupons  
 184 that were immersed for a longer time. Corrosion damages with abrasion were apparent in the  
 185 coupons after 72 and 120 hours of immersion test (Figure 2). Blisters with a width of up to 6 mm were  
 186 also present on the surface of immersed coupons (e.g., the coupon after 120 hours of immersion test;  
 187 Figure 2), and they are probably oxygen corrosion blisters. The coupons after 168 hours of immersion  
 188 further experienced extensive corrosion with most their color turning reddish-brown (Figure 2). By  
 189 visual inspection, however, obvious visual differences were not found between the coupons from the

190 reference fluid and air-nanobubble fluid.

191 Weight losses of the coupons immersed in the reference fluid increased gradually through  
192 time, ranging from 225.8 mg (2.6% of the original mass before immersion test) to 946.4 mg (10.9%).  
193 The weight loss rate in the reference fluid was highest for the coupon immersed for 24 hr (226  
194 mg/day) and the average rate of weight loss 166 mg/day. Similarly, weight losses of the coupons  
195 immersed in the air-nanobubbles fluid also generally increased through time, ranging from 171.2 mg  
196 (2.0% of the original mass before immersion test) to 810.0 mg (9.1%) with the average weight loss  
197 rate of 132 mg/day, while the changes were more fluctuating than those in the reference fluid. The  
198 fluctuation might be due to an unsteady fluid flow rate to the tested container and/or an unsteady  
199 rate of nanobubble generation. Notably, weight losses of the coupons immersed in the air-  
200 nanobubbles fluid after 24, 48, 72, 120, and 168 hours of immersion were significantly smaller than  
201 those in the reference fluid after the respective time of immersion (Figure 3). The corrosion inhibition  
202 effectiveness ( $\eta$ ) of the coupons immersed for 24, 48, 72, 120, and 168 hours was 24%, 21%, 52%,  
203 28%, and 16%, respectively. Only the coupon taken from the air-nanobubbles fluid after 96 hours of  
204 immersion resulted in a larger weight loss than the coupon from the reference fluid after the  
205 respective time of immersion.

206



207

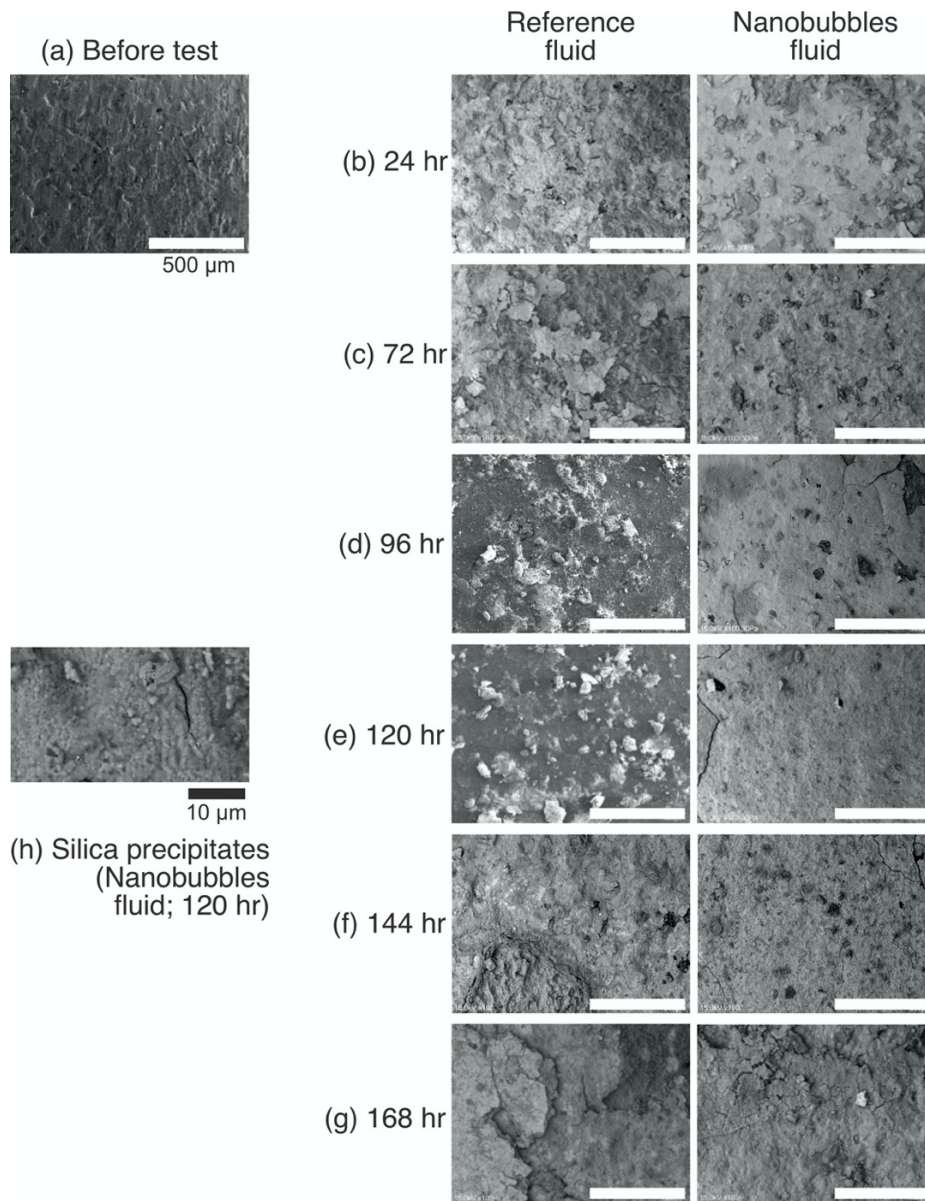
208 Figure 3: Weight changes of the coupons immersed in the reference fluid (red triangles) and air-  
209 nanobubble fluid (blue circles).

210

### 211 3.2. Microstructure and chemical composition on the coupon surfaces

212 Microstructure analyses using SEM revealed in detail corrosion progress in the coupons  
213 immersed in the reference fluid and air-nanobubbles fluid throughout the tested period (Figure 4).  
214 Microstructure analyses showed that the abrasion on the coupon surface was already apparent even  
215 after 24 hours of immersion testing both in the reference fluid and air-nanobubble fluid (Figure 4b).  
216 As suggested by visual observation in Section 3.1, microstructure analyses also indicated that surface

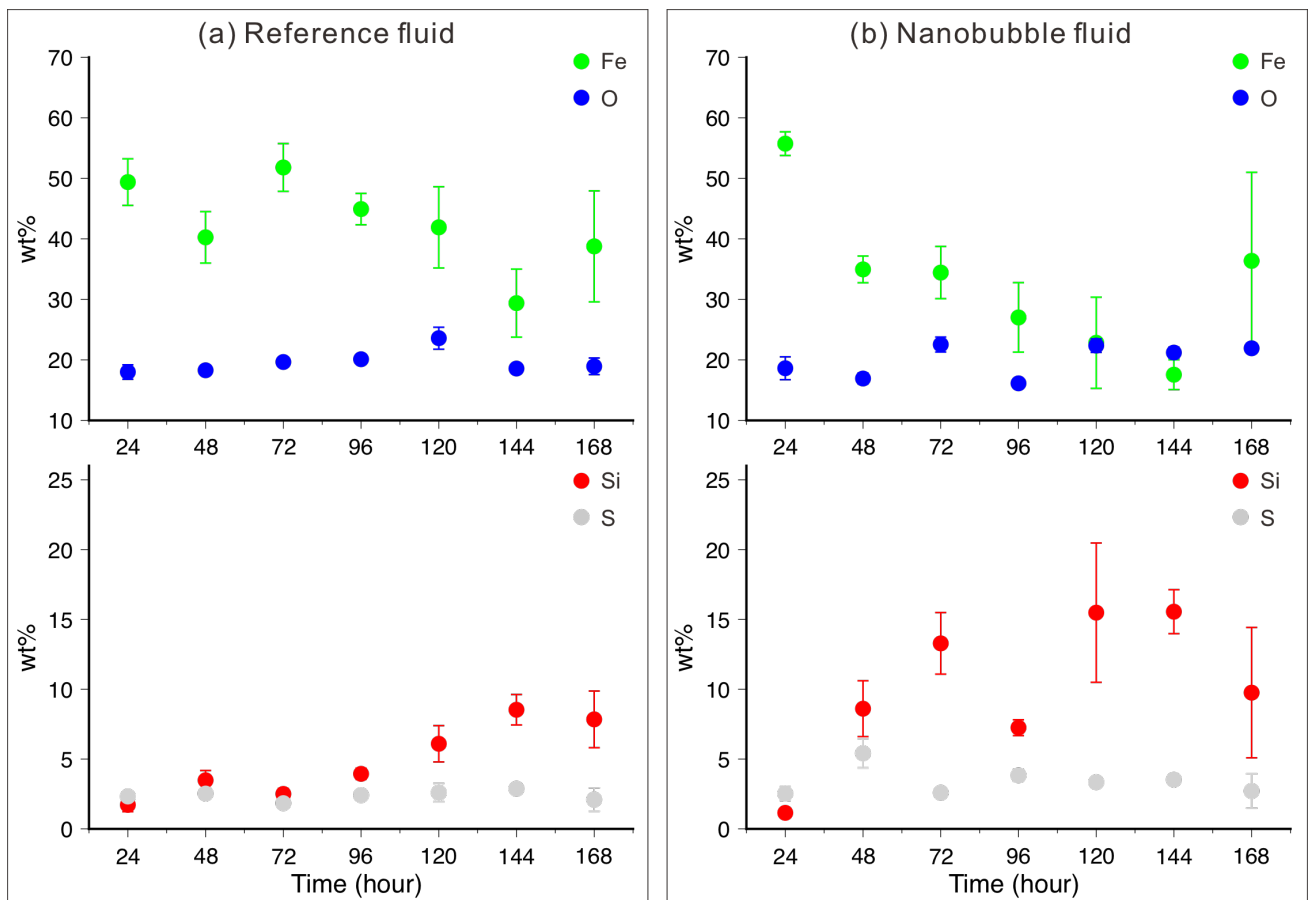
217 abrasion and cracking were further promoted on the coupons that were immersed for a longer time.  
 218 Interestingly, when compared with the coupons after 72, 96, 120, 144, and 168 hours of immersion  
 219 in the reference fluid, the coupons immersed in the air-nanobubbles fluid for the respective time had  
 220 less abrasion (Figures 4c–4g).  
 221



222  
 223 Figure 4: Representative SEM images of the coupons from the reference fluid and air-nanobubble  
 224 fluid (a) before immersion corrosion testing, (b) after 24 hr, (c) 72 hr, (d) 96 hr, (e) 120 hr, (f) 144 hr,  
 225 and (g) 168 hr of immersion. A white scale bar indicates 500 μm. (h) Close-up SEM image of the  
 226 coupon immersed in the air-nanobubble fluid for 120 hr, showing nanoscopic silica precipitates. A  
 227 black scale bar indicates 10 μm.

228  
 229 Microanalyses using EDX identified changes in chemical composition on the coupon surface  
 230 with immersion time (Figure 5). In general, iron (Fe) of the coupon surfaces decreased with immersion

231 time, while Fe of the coupon immersed in the nanobubbles fluid is lower than that of the coupon  
 232 immersed in the reference fluid. This may relate to that surface concentration of iron oxides in the  
 233 coupons immersed in the nanobubbles fluid is lower than that in the reference fluid for 48, 72, 96,  
 234 120, and 144 hours of immersion testing. The EDX results also revealed that silica (Si) concentration  
 235 of the coupon immersed in the reference fluid increased monotonically with time of immersion. On  
 236 the other hand, there was an obvious drop of Si concentration of the coupon immersed in the  
 237 nanobubbles fluid for 96 hours. In general, Si concentrations of the coupons immersed for 48–168  
 238 hours in the nanobubbles fluid were higher than those in the reference fluid, as suggested by SEM  
 239 images (Figure 4h).  
 240



241  
 242 Figure 5: Chemical composition on the surfaces of immersed coupons (wt%) analyzed by EDX. (a)  
 243 Coupons immersed in reference fluid and (b) coupons immersed in air-nanobubble fluid. The  
 244 concentrations Fe, O, Si and S of the coupons before the immersion test analyzed by EDX were  
 245  $92.7 \pm 0.8$ ,  $1.73 \pm 0.07$ ,  $0.0$ ,  $0.12 \pm 0.04$  wt%, respectively.  
 246  
 247  
 248

#### 249 4. DISCUSSION

250 We have examined, for the first time to our knowledge, the behavior of steel corrosion

251 immersed in an acidic geothermal fluid with continuously injected nanobubbles. We found that  
252 nanobubbles generally prevented the coupons from corrosional weight loss. Results of our immersion  
253 corrosion experiments revealed that the weight loss of coupons immersed in the fluid with air-  
254 nanobubbles was reduced as much as 50% of the weight of the coupons in the untreated reference  
255 fluid. In addition, microstructure analyses showed retarded roughness from the surface of the  
256 coupons immersed in the nanobubbles fluid. Chemical composition analyses suggested higher  
257 concentrations of silica in the coupons immersed in the nanobubbles fluid. This should be related to  
258 the unique nature of nanobubbles that leads to influence liquid-steel interface. Yet, the interpretation  
259 of how nanobubbles attribute to these corrosion behaviors may not be unique, because of the  
260 intrinsic complexities of corrosion and nanobubbles. Below, we discuss two aspects of our findings,  
261 and they are (1) possible mechanisms with respect to how nanobubbles inhibit corrosion of low-  
262 carbon steels and (2) how much corrosion inhibition effectiveness of low-carbon steels by  
263 nanobubbles is equivalent to that by chemical adjustment of pH.

#### 264 265 **4.1. Possible mechanisms of inhibiting corrosion by nanobubbles**

##### 266 **4.1.1. Bubble mattress**

267 Gas bubbles can exert a strong influence on the fluid flows along the microstructured  
268 hydrophobic surfaces through changing the friction of liquid flows. Nanobubbles attached to the  
269 surface can have a lifetime of many hours, several days (Weijs and Lohse, 2013) or even a couple of  
270 months (Michailidi et al., 2020) and withstand near-boiling temperatures (Zhang et al., 2014). In  
271 addition, nanobubbles favor staying longer on a rough surface with the help of a pinning force on a  
272 rougher surface (Wang and Bhushan, 2010). These properties benefit in that nanobubbles are much  
273 more stable on the hydrophobic rough surface than larger bubbles are. Surface nanobubbles can  
274 influence the fluid flow along the steel surface for a relatively long time. Therefore, we assume the  
275 nanobubbles generated in our experiments are present on the immersed coupon surfaces at around  
276 80°C for many hours, whereas it is difficult to observe them in situ and in real-time.

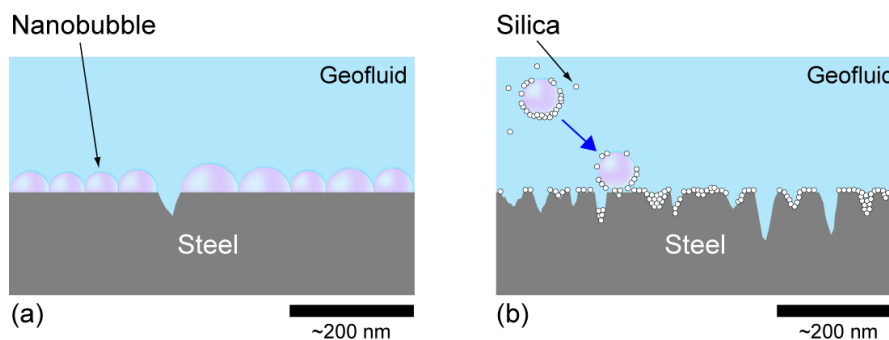
277 Hydrodynamic boundary condition at solid walls is expressed by the Navier boundary  
278 condition. A slip length of a liquid at a solid interface is then expressed through  $u = b(\partial u/\partial z)_0$ ,  
279 where  $u$  is the slip velocity at the solid wall,  $b$  is the slip length, and  $(\partial u/\partial z)_0$  is the velocity  
280 gradient at the wall in the normal direction (Tabeling, 2005). This indicates that a larger slip length  
281 means a lower drag of liquid flow at the interface. The presence of surface nanobubbles on the solid  
282 interface thus affects the slip length. Previous experimental and theoretical studies have shown that  
283 surface nanobubbles affect the slip length on a hydrophobic surface, while the slippage is also  
284 influenced by surface roughness and wettability (Lauga and Stone, 2003; Niavarani and Priezjev, 2010;  
285 Yen, 2015). Also, it is thought that the slip length can be larger in the lower pH solutions that we  
286 studied, due to an increase in concentration of  $H^+$  leading to an increase of the absolute value in  
287 surface charge (Li and Bhushan, 2015).

288 Once a few nanobubbles are present on the steel surface, the slip length may first decrease

289 and the drag force on the steel wall may decrease (Maali and Bhushan, 2013). However, the slip length  
 290 will then increase with an increase of the surface coverage of nanobubbles (Wang and Bhushan, 2010;  
 291 Hyväluoma et al., 2011; Li et al., 2016) and a decrease in the contact angle of nanobubbles on a  
 292 rougher surface (Yen, 2015; Li et al., 2016) due to steel erosion/corrosion, leading to reduce wall  
 293 friction and enhance a wettability on the rough steel surface. After a continuous injection of  
 294 nanobubbles for a certain time, the slip length further increases (Wang and Bhushan, 2010) when  
 295 nanobubbles cover greater parts of the steel surface. Given that the inhibition effectiveness had  
 296 already seen in the first 24 hr of immersion in our testing (Figure 3), nanobubbles had already covered  
 297 most of the steel surface or at least the sufficient area of the surface that could increase the slip  
 298 length within the first 24 hr. In contrast to microbubbles (e.g., Steinberger et al., 2007), we also  
 299 suggest that surface nanobubbles can also act as a bubble mattress on the steel surface (Hyväluoma  
 300 et al., 2011) which isolates the steel surface from the acidic fluid for further corrosion reaction.  
 301 Microbubbles are simply not capable of embracing the interplay between chemical and physical  
 302 alteration of the surface.

303 Nanoscale corrosion pathways could have a profound impact on the corrosion behavior of  
 304 steel. Real-time observations using electron microscopy techniques have been demonstrated that the  
 305 localized corrosion of low-carbon steel initiates at the triple junction formed by an isolated cementite  
 306 inclusion and two abutting ferrite grains. The corrosion is accelerated along the electrochemically  
 307 active interface of these two phases having a relatively long surface contact length of hundreds of  
 308 nanometers (Hayden et al., 2019). Therefore, we would propose that the surface nanobubbles could  
 309 also act as a surface coating material for (1) inhibiting initiation of corrosion at such the physical  
 310 contact by increasing the slip length, and/or (2) preventing from exposing the initiated active interface  
 311 to the acid geothermal fluid by acting as a bubble mattress (Figure 6a). These processes represent an  
 312 important contribution of surface nanobubbles to the material coating at the acidic geothermal  
 313 medium that may have a broader significance.

314



315

316 Figure 6: Schematic illustration of mechanism of inhibiting corrosion by nanobubbles. (a) Bubble  
 317 mattress. (b) Silica precipitation.

318

#### 319 4.1.2. Silica precipitation

320

The studied geothermal fluid contains sufficient concentrations of silica (Table 1). Thus, as

321 an alternative to the aforementioned physical process-based explanation, we also consider that silica  
322 precipitation contributes to inhibiting metallic corrosion in the acidic geothermal fluid. Precipitation  
323 of silica is common in high-enthalpy geothermal power plants, where fluids are rapidly cooled during  
324 geothermal energy production (Corsi, 1986; Gallup, 2009; van den Heuvel et al., 2018). In geothermal  
325 environment, this silica scaling problem is of the same importance of metallic corrosion. On the other  
326 hand, Mundhenk et al. (2013) have suggested that scaling accompanies corrosion of mild steels at  
327 moderate temperatures in geothermal power plants and contributes to the resistance of the  
328 materials. Moreover, several studies have also found that, once an initial layer of amorphous silica  
329 precipitates forms, it probably hampers the underlying steel surface from further reaction with  
330 geothermal fluid (Meier et al., 2014; van den Heuvel et al., 2016). Therefore, silica precipitates may  
331 indeed act as inhibiting corrosion in an acidic moderate-temperature geothermal fluid.

332 Zeta-potential measurements of silica colloids as a function of pH show that the isoelectric  
333 point of silica nanoparticles is close to pH 2 (Xu et al., 2006; Mandel et al., 2015; Alkhamash et al.,  
334 2015; Wang et al., 2017). In the pH of 2 to 6, the zeta potential of silica generally ranges from 0 to -30  
335 mV, indicating the surface of silica is negatively charged and functionalized with Si-O<sup>-</sup> groups (Bai et  
336 al., 2009). In contrast, nanobubbles are generally positively charged in the solutions of pH < 4  
337 (Takahashi, 2005; Calgaroto et al., 2014; Zhu et al., 2016). Surface nanobubbles can thus  
338 electrochemically adsorb nanoparticles (Seo et al., 2007; Berkelaar et al., 2013; Zhou et al., 2019) in  
339 the studied acidic fluid (pH~3.5), resulting in promoting silica polymerisation and/or nucleation of  
340 silica monomers and their succeeding growth on the metallic surface. Therefore, nanobubbles can be  
341 an additive for generating a nano-silica blanket on the metallic surface to isolate the surface from  
342 flowing acidic geothermal water, when precipitated quantities of silica are moderate (Figure 6b).

343 Our EDX analyses showed the enhanced Si concentrations on the coupon surfaces immersed  
344 in the nanobubbles fluid, in comparison to those in the untreated reference fluid (Figure 5), even after  
345 the usual cleaning procedures of coupons (see Section 2.2). In the acidic fluid environment, silica  
346 polymerization is delayed at lower pH (Alexander, 1954; Chan, 1989; Icopini et al, 2005), suggesting  
347 monomeric silica favors in deposition at the studied low pH (pH~3.5). The deposition of amorphous  
348 silica on the coupons might also occur due to that the duration of our immersion experiment is longer  
349 than the silica induction period at the studied pH. Although it is difficult to quantify how much silica  
350 is precipitated on the tested coupons, it should be noted that the silica precipitation rates reported  
351 in silica-rich geothermal power plants worldwide fall within 600 and 4500 mg/m<sup>2</sup>/day (e.g., Mroczek  
352 et al., 2017; Okazaki et al., 2017; van den Heuvel et al., 2018). This indicates that silica precipitation  
353 on the surface of the tested coupon (50 mm × 20 mm) could be within 0.6–4.5 mg/day. This number  
354 is well below the absolute values of weight losses in tested coupons (c.f., the weight-loss rates for the  
355 first 24 hr immersion were 226 and 171 mg/day in the reference fluid and the nanobubbles fluid,  
356 respectively; Figure 3). Thus, the weight gain in coupons related to silica precipitation is negligible,  
357 while this slight amount of silica precipitation on the coupon surface could play a crucial role for  
358 inhibiting corrosion through generating a silica blanket in the nanobubbles fluid. Our EDX results also

359 showed silica concentrations both in the reference fluid and nanobubbles fluid were quite low in the  
360 first 24 hours of immersion, compared with those in 48–168 hours of immersion (Figure 5). Moreover,  
361 the coupon immersed in the nanobubbles fluid for 96 hours, showing a relatively low silica  
362 concentration indicative of less silica coating, had no corrosion inhibition effectiveness. Therefore, we  
363 would suggest that corrosion likely took place immediately after immersion of the coupons and  
364 before the initial stages of silica precipitation, and that any further corrosion was stopped or slowed  
365 once a complete layer of silica covered the coupons with the help of nanobubbles. Further  
366 experiments are still necessary to verify this hypothesis, including whether higher concentrations of  
367 nanobubbles cause more silica precipitation, and whether nanobubbles encourage silica precipitation  
368 in different pH environments for inhibiting corrosion.

369

#### 370 **4.1.3. Other mechanisms**

371 Our results of inhibiting corrosion by air-nanobubbles might be counter-intuitive findings,  
372 because injection of air-nanobubbles can be taken as entrapping more oxygen into the geothermal  
373 fluid which could intrusively promote oxygen corrosion. Several works (Ushikubo et al., 2010; Ebina  
374 et al., 2013; Liu et al., 2019) have found that that the nanobubbles generated by oxygen gases increase  
375 dissolved oxygen (DO) concentrations by approximately 500% in an aqueous solution (e.g., from 9  
376 mg/L to 40–45 mg/L in water). Nanobubbles generated by air also can increase DO concentration by  
377 ca. 200% in the geothermal fluid open to the air, taking into account a partial pressure of oxygen in  
378 air. The electrochemical corrosion potential (ECP) of metals in high-temperature fluid increases with  
379 DO concentration (e.g., Kim and Andresen, 2003). This indicates that the increase in ECP associated  
380 with elevated DO concentration can lead the corrosion process into the region of stability of hematite  
381 ( $\text{Fe}_2\text{O}_3$ ), as suggested from the Pourbaix diagram (Beverkog and Puigdomenech, 1996). Several  
382 studies have found that the formation of semi-protective  $\text{Fe}_2\text{O}_3$  on the film in the high-temperature  
383 fluid is encouraged by oxidation of the outer surface of protective magnetite ( $\text{Fe}_3\text{O}_4$ ) due to higher  
384 DO concentration and the resulting ECP elevation (Kumai and Devine, 2007; Kuang et al., 2012; Wang  
385 et al., 2019). Therefore, the elevated DO concentration in the studied fluid due to air-nanobubbles  
386 might lead to lowering corrosion rate through  $\text{Fe}_2\text{O}_3$  formation.

387 It yet remains open to understand whether nanobubbles account for inhibiting corrosion in  
388 different chemical environments, whether nanobubbles-driven corrosion inhibition is dependent on  
389 temperature which influences the stability of nanobubbles (e.g., Berkelaar et al., 2012), and whether  
390 the nanobubbles generated with different gases may respond differently to inhibiting corrosion, while  
391 we studied air-nanobubbles taking into account their low-cost and feasible use. Our results suggest  
392 nanobubbles can inhibit the corrosion due to their intrinsic physicochemical properties, not solely  
393 based on the simple chemical reaction commonly thought. Therefore, we would expect a similar role  
394 in inhibiting corrosion by the nanobubbles generated using different gases, or the nanobubbles  
395 generated by different gases (e.g., nitrogen) could show better corrosion inhibition effectiveness, but  
396 reserve final judgement for the future when further constraints are available. Anyhow, our findings

397 highlight the physicochemical significance of nanobubbles as the coating material in an acidic  
398 geothermal fluid that may have a broader span of significance yet to be discovered.

399

#### 400 **4.2. Effectiveness of corrosion inhibition by nanobubbles**

401 In a geothermal environment, the acceptable corrosion rate for materials is generally  
402 considered to be below 0.1 mm/year, given a certain corrosion allowance and a 20-year life. However,  
403 corrosion in an acidic geothermal fluid environment is much severe, ranging from a couple of  
404 millimeters per year in the moderate fluid environment to more than 100 mm/yr in the high-  
405 temperature and high-fluid velocity environment (Nogara and Zarrouk, 2018b). The pH is known for  
406 being one of the most significant factors determining the magnitude of corrosion in the geothermal  
407 fluid (e.g., Sanada et al., 1995; Yanagisawa et al., 2017). For example, Yanagisawa et al. (2017)  
408 reported the corrosion rate of carbon steel in the geothermal fluid is 1.6 mm/yr at pH 3.6 and 145°C  
409 while the rate is reduced to around 0.1 mm/yr at higher pH of 4.6 and higher temperature of 168°C.  
410 Thus, the pH-adjustment using chemical materials is conventionally one of the common methods for  
411 inhibiting such intensive corrosion, but it can easily change the fluid chemistry which may produce  
412 undesired products. Therefore, there is a demand of the pH-adjustment for corrosion inhibition  
413 without the use of chemical materials. In contrast, we found that nanobubbles as a chemically benign,  
414 environmental-friendly, easy-to-use and low-cost additive agent had good corrosion inhibition  
415 effectiveness, probably by acting as bubble mattress and/or promoting slight precipitation of silica on  
416 the steel surface.

417 Here, we estimate how much corrosion inhibition effectiveness of low-carbon steels by air-  
418 nanobubbles is equivalent to that by pH-adjustment, by simulating long-term corrosion rates. First,  
419 the corrosion rates of immersed coupons can be approximated by the weight loss rate measured in  
420 the immersion corrosion test. A greater weight loss during the test implies higher corrosion rates.  
421 Assuming uniform corrosive recession, the corrosion rate  $C_r(t)$  (mm/year) of the coupon immersed  
422 for  $t$  (hr) is obtained from:

$$423 \quad C_r(t) = \frac{|\Delta m(t)|}{\rho A} \times \frac{24 \times 365}{t},$$

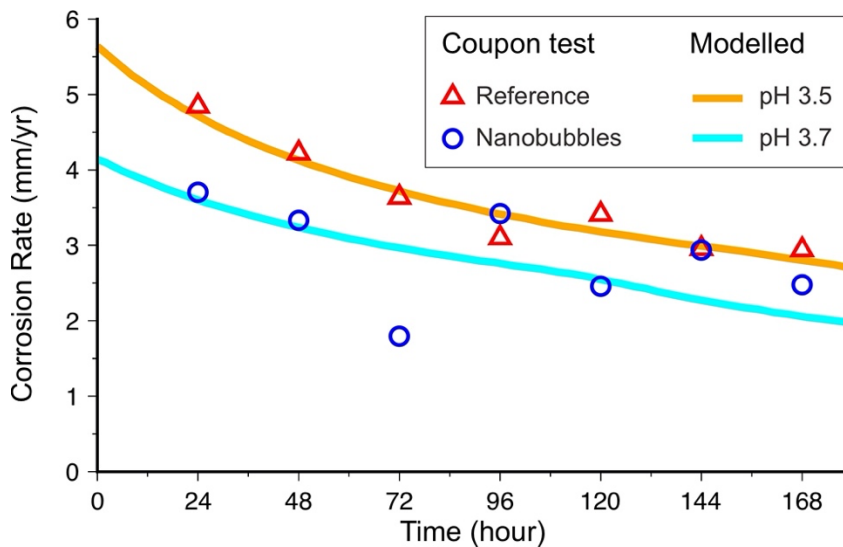
424 where  $\Delta m(t)$  (mg) is the weight loss,  $\rho$  (mg/mm<sup>3</sup>) is the density of mild-steel coupon (7.85  
425 mg/mm<sup>3</sup>), and  $A$  (mm<sup>2</sup>) is the surface area of coupon (ASTM G1-90, 1999). The corrosion rates of  
426 the coupons  $C_r(t)$  immersed in the reference fluid decreased gradually from 4.93 mm/yr to 2.97  
427 mm/yr through time, while those immersed in the nanobubbles fluid ranged from 3.76 mm/yr to 1.78  
428 mm/yr (Figure 7). Second, we used a corrosion model for mild steel in aqueous solutions developed  
429 by Nesic et al. (1996). Here we simulated a time-variable corrosion rate of low-carbon steel for tested  
430 7 days using the software made by Nešić et al. (2009). Because flow properties in immersion  
431 experiments were uncertain, we used the corrosion rates of the coupons immersed in the reference  
432 fluid, an average temperature (80°C) and an average pH value (3.5) and chemical compositions of  
433 studied geothermal fluid (Table 1), to inversely determine the optimum values of flow properties that

434 best fit the corrosion rates of the coupons immersed in the reference fluid. Third, we changed pH  
 435 values to find the optimum pH value that best fits the corrosion rates of the coupons immersed in the  
 436 nanobubbles fluid, while other chemical parameters and flow parameters were unchanged. From this  
 437 calculation, we found the equivalent pH for the corrosion rates of the coupons immersed in the  
 438 nanobubbles fluid was 3.7 (Figure 7). Alternatively, we also estimated the equivalent pH for the  
 439 corrosion rates in the nanobubbles fluid using the relationship among corrosion rate, temperature,  
 440 pH and chemical composition of alloy compiled by Yanagisawa et al. (2017). Using their empirical  
 441 equation, the ratio of corrosion rate in the reference fluid ( $C_{r,Ref}$ ) over the rate in the nanobubble  
 442 fluid ( $C_{r,NB}$ ) under the equal temperature and chemical composition is given by:

$$443 \ln(C_{r,Ref}/C_{r,NB}) = -0.622 \times (\text{pH}_{ref} - \text{pH}_{eq})$$

444 where  $\text{pH}_{ref}$  (= 3.5) and  $\text{pH}_{eq}$  are pH in the reference fluid and the equivalent pH for the corrosion  
 445 rates of the coupons immersed in the nanobubbles fluid, respectively. We could obtain the equivalent  
 446 pH for the corrosion rates in the nanobubbles fluid ( $\text{pH}_{eq}$ ) was 3.9–4.0 based on the results for 24 hr,  
 447 48 hr and 120 hr. From these calculations, we suggest that our chemically-benign air-nanobubble  
 448 treatment in the acidic geothermal fluid is comparable to neutralizing 0.2–0.5 in pH by pH-adjustment  
 449 using chemical materials.

450



451

452 Figure 7: Corrosion rates of the coupons immersed in the reference fluid (red triangles) and the  
 453 nanobubbles fluid (blue circles) with modelled corrosion rates at pH of 3.5 (orange line) and 3.7 (cyan  
 454 line).

455

456

457

## 458 5. CONCLUSIONS

459

460 We studied the use of nanobubbles as a corrosion inhibitor, for the first time to our  
 knowledge, by testing immersion corrosion of low-carbon steel coupons in acidic geothermal fluid

461 on-site a geothermal power plant. We performed weight loss measurements of the coupons  
462 immersed in the untreated geothermal fluid and the geothermal fluid with continuous injection of  
463 the air-nanobubbles for 7 days, and analyzed microstructure and chemical composition of the coupon  
464 surfaces using SEM and EDX, respectively. Together with the results, we found that air-nanobubbles  
465 could inhibit the corrosion of low-carbon steels, with inhibition efficiency of 20–50% in the studied  
466 acidic geothermal fluid. We concluded that air-nanobubbles could act as a nanoscopic coating  
467 material in mitigating corrosion, for increasing the slip length on the solid interface and/or preventing  
468 from exposing the interface to acidic geothermal fluid, by (1) behaving as a bubble mattress which  
469 covered most the steel surface and/or (2) promoting nucleation and aggregation of a very small  
470 quantity of silica precipitation on the steel surface. Our finding suggests that nanobubbles can inhibit  
471 steel corrosion in various chemically different geothermal fluids, highlighting the physicochemical  
472 significance of nanobubbles as the coating material for nanoscopically mitigating metallic degradation  
473 in geothermal infrastructures.

474

475

476

#### 477 **Data Availability**

478 All data used in this work required to reproduce the results presented can be provided upon  
479 request to the corresponding author.

480

#### 481 **Declaration of Competing Interest**

482 The authors declare that they have no known competing financial interests or personal  
483 relationships that could have appeared to influence the work reported in this paper.

484

#### 485 **Authorship contribution statement**

486 **Asuki Aikawa:** Data curation, Resources, Formal analysis, Investigation, Methodology, Validation,  
487 Visualization, Writing – original draft. **Arata Kioka:** Conceptualization, Data curation, Resources,  
488 Formal analysis, Investigation, Funding acquisition, Methodology, Validation, Visualization, Writing –  
489 original draft, Supervision. **Masami Nakagawa:** Conceptualization, Resources, Investigation, Funding  
490 acquisition, Project administration, Writing – review & editing, Supervision. **Satoshi Anzai:** Resources,  
491 Methodology.

492

#### 493 **Acknowledgment**

494 The authors are grateful to A. Ueda, T. Yokoyama, R. Itoi, K. Yonezu, Y. Kiyota, K. Tagomori,  
495 and T. Kodama for discussion and their help throughout the work presented in the manuscript. The  
496 manuscript benefited from constructive comments by three anonymous reviewers. This work was  
497 partly supported by the project “Research and development of geothermal power generation  
498 technology — Development of technology for advanced use of geothermal energy — Development

499 of chemical processing systems to properly utilize and brine” from the New Energy and Industrial  
500 Technology Development Organization (NEDO), Japan. A.K. acknowledges financial support from the  
501 New Frontiers in Engineering Research, Kyushu University (FY2020-2021).

502

503

## 504 REFERENCES

505 Alexander, G.B., 1954. The Polymerization of Monosilicic Acid. *J. Am. Chem. Soc.* 76, 2094–2096.  
506 <https://doi.org/10.1021/ja01637a017>

507 Alkhamash, H.I., Li, N., Berthier, R., de Planque, M.R.R., 2015. Native silica nanoparticles are  
508 powerful membrane disruptors. *Phys. Chem. Chem. Phys.* 17, 15547–15560.

509 <https://doi.org/10.1039/C4CP05882H>

510 ASTM G1-90, 1999. Standard Practice for Preparing, Cleaning, and Evaluating Corrosion Test  
511 Specimens. West Conshohocken, PA: ASTM.

512 ASTM G4-01, 2008. Standard Guide for Conducting Corrosion Tests in Field Applications. West  
513 Conshohocken, PA: ASTM.

514 Bai, S., Urabe, S., Okaue, Y., Yokoyama, T., 2009. Acceleration effect of sulfate ion on the dissolution  
515 of amorphous silica. *J. Colloid Interf. Sci.* 331, 551–554.

516 <https://doi.org/10.1016/j.jcis.2008.11.076>

517 Berkelaar, R.P., Seddon, J.R.T., Zandvliet, H.J.W., Lohse, D., 2012. Temperature Dependence of  
518 Surface Nanobubbles. *ChemPhysChem* 13, 2213–2217.

519 <https://doi.org/10.1002/cphc.201100808>

520 Berkelaar, R.P., Zandvliet, H.J.W., Lohse, D., 2013. Covering Surface Nanobubbles with a NaCl  
521 Nanoblanket. *Langmuir* 29, 11337–11343. <https://doi.org/10.1021/la402503f>

522 Beverskog, B., Puigdomenech, I., 1996. Revised pourbaix diagrams for iron at 25–300°C. *Corros. Sci.*  
523 38, 2121–2135. [https://doi.org/10.1016/S0010-938X\(96\)00067-4](https://doi.org/10.1016/S0010-938X(96)00067-4)

524 Calgaroto, S., Wilberg, K.Q., Rubio, J., 2014. On the nanobubbles interfacial properties and future  
525 applications in flotation. *Miner. Eng.* 60, 33–40. <http://dx.doi.org/10.1016/j.mineng.2014.02.002>

526 Chan, S.H., 1989. A review on solubility and polymerization silica. *Geothermics* 18, 49–56.

527 [https://doi.org/10.1016/0375-6505\(89\)90009-6](https://doi.org/10.1016/0375-6505(89)90009-6)

528 Corsi, R., 1986. Scaling and corrosion in geothermal equipment: problems and preventive measures.  
529 *Geothermics* 15 (5–6), 839–856. [https://doi.org/10.1016/0375-6505\(86\)90097-0](https://doi.org/10.1016/0375-6505(86)90097-0)

530 Dwivedi, D., Lepková, K., Becker, T., 2017. Carbon steel corrosion: a review of key surface properties  
531 and characterization methods. *RSC Adv.* 7, 4580–4610. <https://doi.org/10.1039/C6RA25094G>

532 Ebina, K., Shi, K., Hirao, M., Hashimoto, J., Kawato, Y., Kaneshiro, S., Morimoto, T., Koizumi, K.,  
533 Yoshikawa, H., 2013. Oxygen and Air Nanobubble Water Solution Promote the Growth of Plants,  
534 Fishes, and Mice. *PLOS ONE* 8(6), e65339. <https://doi.org/10.1371/journal.pone.0065339>

535 El-Hajjaji, F., Messali, M., Martínez de Yuso, M.V., Rodríguez-Castellón, E., Almutairi, S., Bandosz, T.J.,  
536 Algarra, M., 2019. Effect of 1-(3-phenoxypropyl) pyridazin-1-ium bromide on steel corrosion

537 inhibition in acidic medium. *J. Colloid Interf. Sci.* 541, 418–424.  
538 <https://doi.org/10.1016/j.jcis.2019.01.113>

539 Finšgar, M., Jackson, J., 2014. Application of corrosion inhibitors for steels in acidic media for the oil  
540 and gas industry: A review. *Corros. Sci.* 86, 17–41. <https://doi.org/10.1016/j.corsci.2014.04.044>

541 Gallup, D.L., 2009. Production engineering in geothermal technology: A review. *Geothermics* 38,  
542 326–334. <https://doi.org/10.1016/j.geothermics.2009.03.001>

543 Hayden, S.C., Chisholm, C., Grudt, R.O., Aguiar, J.A., Mook, W.M., Kotula, P.G., Pilyugina, T.S.,  
544 Bufford, D.C., Hattar, K., Kucharski, T.J., Taie, I.M., Ostraat, M.L., Jungjohann, K.L., 2019. Localized  
545 corrosion of low-carbon steel at the nanoscale. *npj Mater. Degrad.* 3, 17.  
546 <https://doi.org/10.1038/s41529-019-0078-1>

547 Hyväluoma, J., Kunert, C., Harting, J., 2011. Simulations of slip flow on nanobubble-laden surfaces. *J.*  
548 *Phys. Condens. Matter* 23, 184106. <https://doi.org/10.1088/0953-8984/23/18/184106>

549 Icopini, G.A., Brantley, S.L., Heaney, P.J., 2005. Kinetics of silica oligomerization and nanocolloid  
550 formation as a function of pH and ionic strength at 25°C. *Geochim. Cosmochim. Acta* 69, 293–  
551 303. <https://doi.org/10.1016/j.gca.2004.06.038>

552 Kim, Y.-J., Andresen, P.L., 2003. Data Quality, Issues, and Guidelines for Electrochemical Corrosion  
553 Potential Measurement in High-Temperature Water. *Corrosion* 59, 584–596.  
554 <https://doi.org/10.5006/1.3277589>

555 Kuang, W., Wu, X., Han, E.-H., 2012. Influence of dissolved oxygen concentration on the oxide film  
556 formed on 304 stainless steel in high temperature water. *Corros. Sci.* 63, 259–266.  
557 <https://doi.org/10.1016/j.corsci.2012.06.007>

558 Kumai, C.S., Devine, T.M., 2007. Influence of Oxygen Concentration of 288°C Water and Alloy  
559 Composition on the Films Formed on Fe-Ni-Cr Alloys. *Corrosion* 63, 1101–1113.  
560 <https://doi.org/10.5006/1.3278328>

561 Lauga, E., Stone, H.A., 2003. Effective slip in pressure-driven Stokes flow. *J. Fluid Mech.* 489, 55–77.  
562 <https://doi.org/10.1017/S0022112003004695>

563 Li, D., Jing, D., Pan, Y., Bhushan, B., Zhao, X., 2016. Study of the Relationship between Boundary Slip  
564 and Nanobubbles on a Smooth Hydrophobic Surface. *Langmuir* 32(43), 11287–11294.  
565 <https://doi.org/10.1021/acs.langmuir.6b02877>

566 Li, Y., Bhushan, B., 2015. The effect of surface charge on the boundary slip of various  
567 oleophilic/phobic surfaces immersed in liquid. *Soft Matter* 11, 7680–7695.  
568 <https://doi.org/10.1039/C5SM00763A>

569 Liu, Y., Zhou, Y., Wang, T., Pan, J., Zhou, B., Muhammad, T., Zhou, C., Li, Y., 2019. Micro-nano bubble  
570 water oxygation: Synergistically improving irrigation water use efficiency, crop yield and quality.  
571 *J. Clean. Prod.* 222, 835–843. <https://doi.org/10.1016/j.jclepro.2019.02.208>

572 Lohse, D., Zhang, X., 2015. Surface nanobubbles and nanodroplets. *Rev. Mod. Phys.* 87, 981–1035.  
573 <https://doi.org/10.1103/RevModPhys.87.981>

574 Maali, A., Bhushan, B., 2013. Nanobubbles and their role in slip and drag. *J. Phys. Condens. Matter*

575 25, 184003. <https://doi.org/10.1088/0953-8984/25/18/184003>

576 Mandel, K., Straßer, M., Granath, T., Dembski, S., Sextl, G., 2015. Surfactant free superparamagnetic  
577 iron oxide nanoparticles for stable ferrofluids in physiological solutions. *Chem. Commun.* 51,  
578 2863-2866. <https://doi.org/10.1039/C4CC09277E>

579 Meier, D., Gunnlaugsson, E., Gunnarsson, I., Jamtveit, B., Peacock, C., Benning, L., 2014.  
580 Microstructural and chemical variation in silica-rich precipitates at the Hellisheiði geothermal  
581 power plant. *Mineral. Mag.* 78(6), 1381–1389. <https://doi.org/10.1180/minmag.2014.078.6.04>

582 Michailidi, E.D., Bomis, G., Varoutoglou, A., Kyzas, G.Z., Mitrikas, G., Mitropoulos, A.Ch.,  
583 Efthimiadou, E.K., Favvas, E.P., 2020. Bulk nanobubbles: Production and investigation of their  
584 formation/stability mechanism. *J. Colloid Interf. Sci.* 564, 371–380.  
585 <https://doi.org/10.1016/j.jcis.2019.12.093>

586 Mroczek, E., Graham, D., Siega, C., Bacon, L., 2017. Silica scaling in cooled silica saturated  
587 geothermal water: Comparison between Wairakei and Ohaaki geothermal fields, New Zealand.  
588 *Geothermics* 69, 145–152. <https://doi.org/10.1016/j.geothermics.2017.05.006>

589 Mundhenk, N., Huttenloch, P., Sanjuan, B., Kohl, T., Steger, H., Rorn, R., 2013. Corrosion and scaling  
590 as interrelated phenomena in an operating geothermal power plant. *Corros. Sci.* 70, 17–28.  
591 <https://doi.org/10.1016/j.corsci.2013.01.003>

592 Nestic, S., Postlethwaite, J., Olsen, S., 1996. An Electrochemical Model for Prediction of Corrosion of  
593 Mild Steel in Aqueous Carbon Dioxide Solutions. *Corrosion* 52(4), 280–294.  
594 <https://doi.org/10.5006/1.3293640>

595 Nešić, S., Li, H., Huang, J., Sormaz, D., 2009. An Open Source Mechanistic Model for CO<sub>2</sub>/H<sub>2</sub>S  
596 Corrosion of Carbon Steel. NACE International Corrosion/09, Houston, TX, paper no. 09572.

597 Niavarani, A., Priezjev, N.V., 2010. Modeling the combined effect of surface roughness and shear  
598 rate on slip flow of simple fluids. *Phys. Rev. E* 81, 011606.  
599 <https://doi.org/10.1103/PhysRevE.81.011606>

600 Nogara, J., Zarrouk, S.J., 2018a. Corrosion in geothermal environment: Part 1: Fluids and their  
601 impact. *Renew. Sust. Energ. Rev.* 82, 1333–1346. <https://doi.org/10.1016/j.rser.2017.06.098>

602 Nogara, J., Zarrouk, S.J., 2018b. Corrosion in geothermal environment: Part 2: Metals and alloys.  
603 *Renew. Sust. Energ. Rev.* 82, 1347–1363. <https://doi.org/10.1016/j.rser.2017.06.091>

604 Okazaki, T., Orii, T., Ueda, A., Ozawa, A., Kuramitz, H., 2017. Fiber Optic Sensor for Real-Time Sensing  
605 of Silica Scale Formation in Geothermal Water. *Sci. Rep.* 7, 3387.  
606 <https://doi.org/10.1038/s41598-017-03530-1>

607 Sanada, N., Kurata, Y., Nanjo, H., Ikeuchi, J., 1995. Material damage in high velocity acidic fluids. *GRC*  
608 *Trans.* 19, 359–363.

609 Seo, H., Yoo, M., Jeon, S., 2007. Influence of Nanobubbles on the Adsorption of Nanoparticles.  
610 *Langmuir* 23, 1623–1625. <https://doi.org/10.1021/la062763r>

611 Shokry, H., Yuasa, M., Sekine, I., Issa, R.M., El-baradie, H.Y., Gomma, G.K., 1998. Corrosion inhibition  
612 of mild steel by schiff base compounds in various aqueous solutions: part 1. *Corros. Sci.* 40 (12),

613 2173–2186. [https://doi.org/10.1016/S0010-938X\(98\)00102-4](https://doi.org/10.1016/S0010-938X(98)00102-4)

614 Solomon, M.M., Umoren, S.A., Quraishi, M.A., Salman, M., 2019. Myristic acid based imidazoline  
615 derivative as effective corrosion inhibitor for steel in 15% HCl medium. *J. Colloid Interf. Sci.* 551,  
616 47–60. <https://doi.org/10.1016/j.jcis.2019.05.004>

617 Steinberger, A., Cottin-Bizonne, C., Kleimann, P., Charlaix, C., 2007. High friction on a bubble  
618 mattress. *Nature Mater.* 6, 665–668. <https://doi.org/10.1038/nmat1962>

619 Sun, W., Liu, Y., Li, T., Cui, S., Chen, S., Yu, Q., Wang, D., 2019. Anti-corrosion of amphoteric metal  
620 enhanced by MAO/corrosion inhibitor composite in acid, alkaline and salt solution. *J. Colloid  
621 Interf. Sci.* 554, 488–499. <https://doi.org/10.1016/j.jcis.2019.07.035>

622 Tabeling, P., 2005. *Introduction to Microfluidics*. Oxford University Press, UK, 310 p.

623 Takahashi, M., 2005.  $\zeta$  Potential of Microbubbles in Aqueous Solutions: Electrical Properties of the  
624 Gas-Water Interface. *J. Phys. Chem. B* 109, 21858–21864. <https://doi.org/10.1021/jp0445270>

625 Tang, Z., 2019. A review of corrosion inhibitors for rust preventative fluids. *Curr. Opin. Solid State  
626 Mater. Sci.* 23, 100759. <https://doi.org/10.1016/j.cossms.2019.06.003>

627 Tiu, B.D.B., Advincula, R. C., 2015. Polymeric corrosion inhibitors for the oil and gas industry: Design  
628 principles and mechanism. *React. Funct. Polym.* 95, 25–45.  
629 <https://doi.org/10.1016/j.reactfunctpolym.2015.08.006>

630 Ushikubo, F.Y., Furukawa, T., Nakagawa, R., Enari, M., Makino, Y., Kawagoe, Y., Shiina, T., Oshita, S.,  
631 2010. Evidence of the existence and the stability of nano-bubbles in water. *Colloids Surf. A  
632 Physicochem. Eng. Asp.* 361, 31–37. <https://doi.org/10.1016/j.colsurfa.2010.03.005>

633 van den Heuvel, D.B., Gunnlaugsson, E., Benning, L.G., 2016. Passivation of metal surfaces against  
634 corrosion by silica scaling. *Proceedings of the 41st Workshop on Geothermal Reservoir  
635 Engineering, SGP-TR-209*.

636 van den Heuvel, D.B., Gunnlaugsson, E., Gunnarsson, I., Stawski, T.M., Peacock, C.L., Benning, L.G.,  
637 2018. Understanding amorphous silica scaling under well-constrained conditions inside  
638 geothermal pipelines. *Geothermics* 76, 231–241.  
639 <https://doi.org/10.1016/j.geothermics.2018.07.006>

640 Wang, S., Yin, X., Zhang, H., Liu, D., Dun, N., 2019. Coupling Effects of pH and Dissolved Oxygen on  
641 the Corrosion Behavior and Mechanism of X80 Steel in Acidic Soil Simulated Solution. *Materials*  
642 12, 3175. <https://doi.org/10.3390/ma12193175>

643 Wang, X., Shi, L., Zhang, J., Cheng, J., Wang, X., 2017. Self-assembly fabrication, microstructures and  
644 antibacterial performance of layer-structured montmorillonite nanocomposites with cationic  
645 silica nanoparticles. *RSC Adv.* 7, 31502–31511. <https://doi.org/10.1039/C7RA04353H>

646 Wang, Y., Bhushan, B., 2010. Boundary slip and nanobubbles study in micro/nanofluidics using  
647 atomic force microscopy. *Soft Matter* 6, 29–66. <https://doi.org/10.1039/B917017K>

648 Weijs, J.H., Lohse, D., 2013. Why Surface Nanobubbles Live for Hours. *Phys. Rev. Lett.* 110, 054501.  
649 <https://doi.org/10.1103/PhysRevLett.110.054501>

650 Xu, P., Wang, H., Tong, R., Du, Q., Zhong, W., 2006. Preparation and morphology of SiO<sub>2</sub>/PMMA

651 nanohybrids by microemulsion polymerization. *Colloid. Polym. Sci.* 284, 755–762.  
652 <https://doi.org/10.1007/s00396-005-1428-9>

653 Yanagisawa, N., Masuda, Y., Osato, K., Sato, M., Kasai, K., Sakura, K., Fukui, T., 2017. The Material  
654 Corrosion Test Using Small Loop System at Geothermal Power Plant in Japan. *Proceedings of the*  
655 *42nd Workshop on Geothermal Reservoir Engineering*, SGP-TR-212.

656 Yen, T.-H., 2015. Effects of wettability and interfacial nanobubbles on flow through structured  
657 nanochannels: an investigation of molecular dynamics. *Mol. Phys.* 113, 3783–3795.  
658 <https://doi.org/10.1080/00268976.2015.1062928>

659 Zhang, X., Lhuissier, H., Sun, C., Lohse, D., 2014. Surface Nanobubbles Nucleate Microdroplets. *Phys.*  
660 *Rev. Lett.* 112, 144503. <https://doi.org/10.1103/PhysRevLett.112.144503>

661 Zhou, W., Niu, J., Xiao, W., Ou, L., 2019. Adsorption of bulk nanobubbles on the chemically surface-  
662 modified muscovite minerals. *Ultrason. Sonochem.* 51, 31–39.  
663 <https://doi.org/10.1016/j.ultsonch.2018.10.021>

664 Zhu, J., An, H., Alheshibri, M., Liu, L., Terpstra, P.M.J., Liu, G., Craig, V.S.J., 2016. Cleaning with Bulk  
665 Nanobubbles. *Langmuir* 32, 11203–11211. <https://doi.org/10.1021/acs.langmuir.6b01004>